



A Breakout Model for Solar Coronal Jets with Filaments

P. F. Wyper¹ , C. R. DeVore² , and S. K. Antiochos²

¹ Department of Mathematical Sciences, Durham University, Durham, DH1 3LE, UK; peter.f.wyper@durham.ac.uk

² Heliophysics Science Division, NASA Goddard Space Flight Center, 8800 Greenbelt Road, Greenbelt, MD 20771, USA

c.richard.devore@nasa.gov, spiro.antiochos@nasa.gov

Received 2017 September 7; revised 2017 November 21; accepted 2017 November 30; published 2018 January 11

Abstract

Recent observations have revealed that many solar coronal jets involve the eruption of miniature versions of large-scale filaments. Such “mini-filaments” are observed to form along the polarity inversion lines of strong, magnetically bipolar regions embedded in open (or distantly closing) unipolar field. During the generation of the jet, the filament becomes unstable and erupts. Recently we described a model for these mini-filament jets, in which the well-known magnetic-breakout mechanism for large-scale coronal mass ejections is extended to these smaller events. In this work we use 3D magnetohydrodynamic simulations to study in detail three realizations of the model. We show that the breakout-jet generation mechanism is robust and that different realizations of the model can explain different observational features. The results are discussed in relation to recent observations and previous jet models.

Key words: magnetic reconnection – Sun: corona – Sun: flares – Sun: magnetic fields

Supporting material: animations

1. Introduction

Coronal jets are transient, collimated ejections of plasma launched from low in the solar atmosphere outward along the ambient magnetic field of the corona. Jets occur prolifically across the solar surface, most notably within coronal holes and around the periphery of active regions (Shimojo et al. 1996; Savcheva et al. 2007). They are observed in X-rays (e.g., Shimojo et al. 1996; Cirtain et al. 2007) and at a variety of extreme-ultraviolet (EUV) wavelengths (e.g., Nisticò et al. 2009; Zhang et al. 2016), reflecting the fact that some jets possess both hot and cool (relative to the ambient corona) components. Some jets are energetic enough to reach the heliosphere and become visible as jet-like coronal mass ejections (CMEs) in white-light coronagraphs (e.g., Wang et al. 1998; Patsourakos et al. 2008; Hong et al. 2011; Moore et al. 2015). From X-ray observations, Savcheva et al. (2007) found that a sample of around 100 jets had typical lifetimes of around 10 minutes, lengths on the order of 50 Mm, widths of around 8 Mm, and bulk outflow velocities of around 200 km s^{−1}. For a comprehensive review of jet observations, morphologies, and previous numerical modeling see Raouafi et al. (2016).

Common to all jets is an impulsive release of energy as the jet is launched, accompanied by the formation of hot magnetic loops off to one side of the jet base. Shibata et al. (1992) proposed that the plasma jet and the bright loops (also called the jet bright point) could be explained by the emergence of a small bipole into a unipolar region of open (or distantly closing) magnetic field. External reconnection between the emerging flux and the ambient field would produce a jet of plasma and form a new set of hot, reconnected loops. Numerous numerical experiments have tested this idea and shown that such a jet outflow with loops can be realized from that scenario (e.g., Yokoyama & Shibata 1995, 1996; Miyagoshi & Yokoyama 2003, 2004; Archontis et al. 2005, 2010; Galsgaard et al. 2005; Moreno-Insertis et al. 2008; Gontikakis et al. 2009).

Many jets exhibit the classic inverted-Y, or Eiffel tower, shape consistent with the Shibata picture. However, a large proportion of jets instead have a broad jet spire that often exhibits strong helical motion (e.g., Patsourakos et al. 2008; Nisticò et al. 2009; Shen et al. 2011; Hong et al. 2013; Moore et al. 2015). The prevalence of different jet morphologies was studied by Nisticò et al. (2009) using EUV observations from the *Solar Terrestrial Relations Observatory*. From a sample of 79 jets, their study classified 31 as exhibiting observable helical motions; structurally, 37 were of Eiffel tower type, 12 were of the similar lambda type, 5 resembled miniature CMEs, and the remaining 25 were ambiguous.

Some authors have noted that most jets with helical motions seem to involve the eruption, or blowing out, of the bipole region in a form reminiscent of mini-CMEs (Innes et al. 2009, 2010; Nisticò et al. 2009; Moore et al. 2010; Raouafi et al. 2010). Moore et al. (2010) suggested that such “blowout” jets could be explained by an extension of the Shibata “standard” jet in which the emerging bipole becomes unstable, a section of it erupts, and flare-like loops form underneath to create the jet bright point. Several numerical experiments have now replicated this behavior when the flux emergence continues over a sufficiently long period (e.g., Archontis & Hood 2013; Moreno-Insertis & Galsgaard 2013; Fang et al. 2014).

However, recent observations suggest that flux emergence is not the fundamental driver of all coronal jets. In jets where magnetogram data are available, it is often observed that little or no flux emergence occurs leading up to or during the jet (e.g., Chandrasekhar et al. 2014; Hong et al. 2016). More typically, flux is actually canceling at the base of the jet (e.g., Chae et al. 1999; Hong et al. 2011; Liu et al. 2011; Adams et al. 2014; Young & Muglach 2014a, 2014b; Panesar et al. 2016). Therefore, while flux emergence is highly likely to account for the generation of some coronal jets, it seems improbable that it explains all such events.

A particular challenge to the the flux emergence model is posed by the relatively recent identification in many jets of

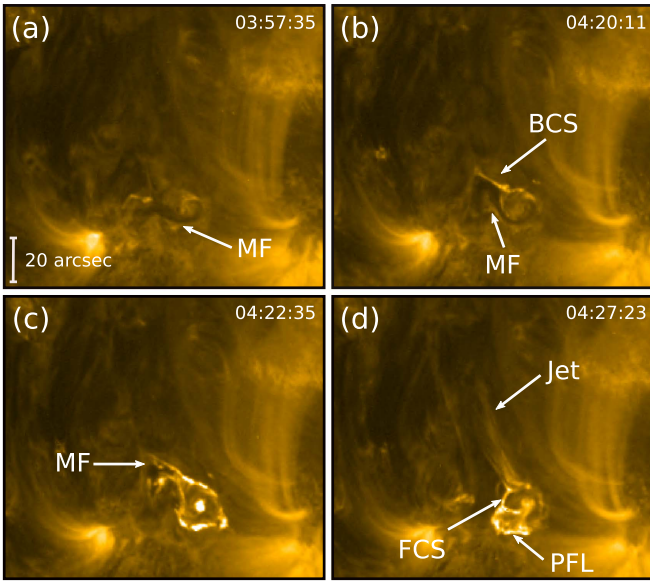


Figure 1. Example of a mini-filament jet. MF = mini-filament; BCS = breakout current sheet; FCS = flare current sheet; PFL = post-flare loops. See the text for details.

small filament-like structures that are invisible in X-rays but can be seen in wavelengths associated with cooler plasma, such as EUV and $H\alpha$ (e.g., Zheng et al. 2012; Sterling et al. 2015; Hong et al. 2016; Zhang et al. 2016). These “mini-filaments” are observed along and above the polarity inversion lines (PILs) of preexisting strong bipoles (e.g., Chae et al. 1999; Hong et al. 2011, 2014, 2016; Zheng et al. 2012; Adams et al. 2014; Panesar et al. 2016; Zhang et al. 2016). They contain cool, dense plasma (relative to the ambient corona) and resemble the large-scale filaments that erupt as CMEs, leaving behind arcades of bright flare loops. In an apparently similar manner, these mini-filaments erupt and leave behind the loops of the jet bright point, as the jet itself propagates away through the corona. The ejection of cool filament material alongside hot plasma heated by reconnection may explain the often-observed simultaneous occurrence of hot jets and their cooler counterparts, surges (e.g., Canfield et al. 1996).

An example of a mini-filament jet in a quiet-Sun region (one of several studied by Panesar et al. 2016) is shown in Figure 1, depicting the typical phases of evolution. The EUV images were taken with the Atmospheric Imaging Assembly aboard the *Solar Dynamics Observatory* at 171 Å ($T \approx 0.7$ MK) on 2012 November 13 and were rendered using Helioviewer (<http://www.helioviewer.org>). Prior to the jet, a preexisting, dark mini-filament is present (panel (a)). The overlying structure then slowly begins to rise as a bright linear feature, which we interpret as showing that the breakout current layer (see later sections) forms above it (panel (b)). An explosive change in evolution occurs as the dark mini-filament reaches the linear feature (panel (c)), after which an untwisting jet is launched (panel (d)). Concurrent with the launching of the jet is the formation of post-flare loops where the mini-filament was present initially. In addition, a second bright linear feature forms, connecting the top of the loops and the untwisting jet curtain, which we interpret as showing the flare current layer (see also later sections).

Recently, Sterling et al. (2015) examined 20 randomly selected jets and found that all involved mini-filaments. The

largest were comparable in size to the closed-field region and erupted to form broad blowout jets with a strongly rotating spire. The smallest were associated with jets exhibiting the classic inverted-Y shape. Sterling et al. concluded that all jets stem from the eruption of mini-filaments and that flux emergence plays little or no role in jet generation.

To date, only one family of jet models has generated jets without flux emergence. In the model pioneered by Pariat and collaborators (Pariat et al. 2009, 2010, 2015, 2016; Dalmasse et al. 2012; Wyper & DeVore 2016; Wyper et al. 2016; Karpen et al. 2017), a single strong-polarity region embedded in an ambient field of opposite sign is slowly rotated to store magnetic free energy and helicity in the corona. Eventually, a kink-like instability induces explosive interchange reconnection between the rotationally sheared closed field and the external, unsheared open field. The resulting jets have a strong rotational component, consistent with blowout jets, along with a broad spire and enhanced density in the jet over and above the coronal background density. These kink-induced jets are one realization of the “sweeping magnetic twist” jet mechanism proposed by Shibata & Uchida (1986), whereby the transfer of twist/shear by reconnection from closed to open field lines drives a rotating jet, as the twist propagates along the ambient field as a nonlinear Alfvén wave. In their original formulation of the model, Shibata & Uchida envisaged this twist to be stored within a filament, as recent observations have now revealed. However, the simulations cited above lack an internal magnetic structure that would support a filament and do not readily explain the observed asymmetry of the hot reconnected loops at the base following the jet generation.

Motivated by the observations of Sterling et al. (2015), we conducted a high-resolution MHD simulation (Wyper et al. 2017) showing how the “magnetic breakout” mechanism (Antiochos et al. 1999) for large-scale CMEs is universal, also explaining small-scale coronal jets involving mini-filaments. In these jets, free energy is stored in the filament channel along the PIL of a bipole embedded in an open ambient magnetic field; the filament subsequently erupts to form a blowout-like untwisting jet. In this paper, we present the details of this model for coronal jets and demonstrate three realizations with ambient fields of different inclinations. The results in each case show that the filament channel field erupts following the onset of a magnetic-breakout reconnection process at the overlying coronal null point, exactly analogous to the breakout mechanism for large-scale filament eruptions and CMEs (Antiochos et al. 1999; MacNeice et al. 2004; Phillips et al. 2005; DeVore & Antiochos 2008; Lynch et al. 2008, 2009; Karpen et al. 2012; Masson et al. 2013). The slow rise of the filament/flux rope prior to the breakout phase, the subsequent fast flare-like reconnection, and the generation of the impulsive untwisting jet are all consistent with the observations of jets associated with mini-filament eruptions (Figure 1).

Section 2 describes the setup of the simulations and the details of the model. In Section 3, we present a schematic outline of the jet mechanism and the different phases of the evolution. Section 4 describes the energies and general morphologies of the simulated jets, while in Section 5 we discuss the various evolutionary phases and the differences between them in detail. In Section 6, we analyze the Poynting and kinetic-energy fluxes transferred by the jet into the corona. Finally, we discuss our findings in Section 7.

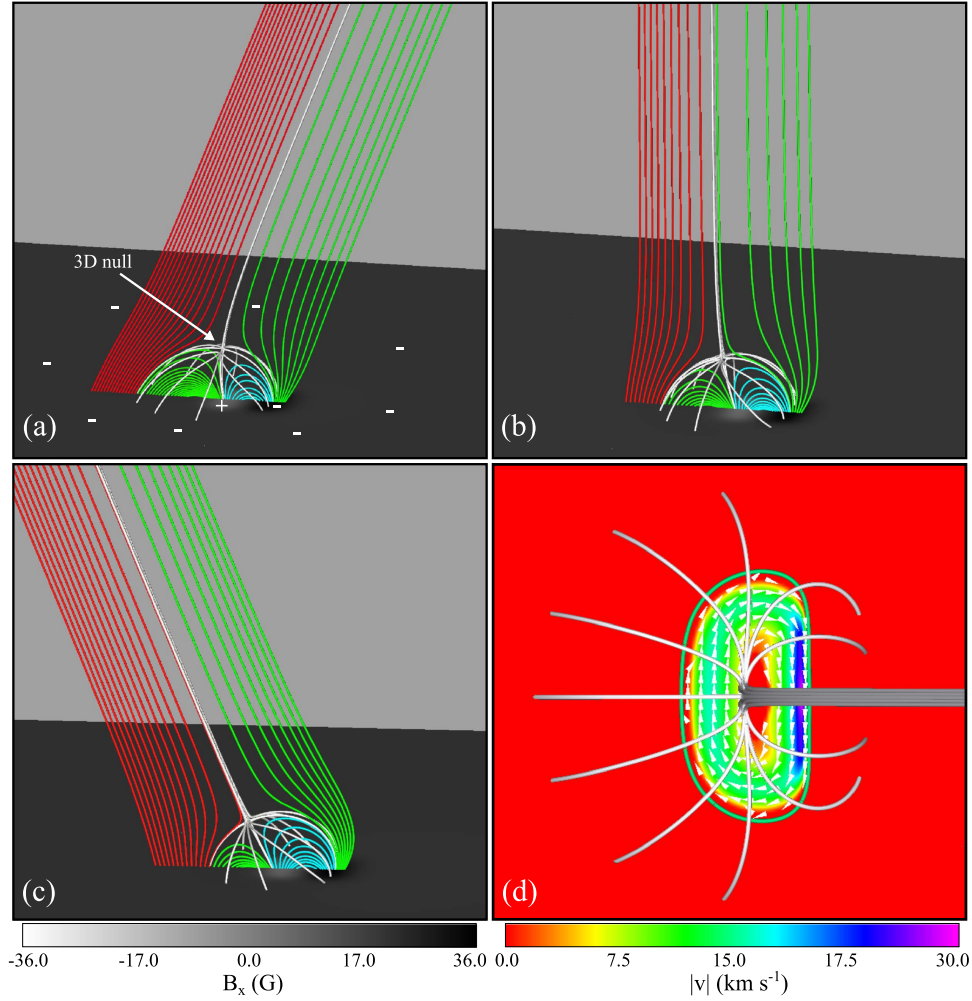


Figure 2. Initial potential magnetic field in the three simulations with background-field tilt angles (a) $\theta = +22^\circ$, (b) $\theta = 0^\circ$, and (c) $\theta = -22^\circ$. The field is composed of the domed fan plane and spine lines (silver field lines) of a 3D coronal null point above the parasitic polarity of a bipolar photospheric flux distribution. (d) Driving flows tangential to the photospheric boundary follow the contours of the positive parasitic polarity and are shown for $\theta = +22^\circ$. Note the increased flow speed near the polarity inversion line (green contour of $B_x = 0$) in the center of the bipolar distribution.

2. Simulation Setup

Observations suggest that the mini-filament erupting in conjunction with a coronal jet is confined beneath closed small-scale coronal loops, which in turn are embedded in the open field along which the jet subsequently propagates. This is highly suggestive of a filament channel forming and subsequently erupting from the closed field beneath an overlying coronal null point. To model this process, we adopt an initially potential field with a compact bipolar structure on the solar surface (where the filament channel will be formed) embedded within a uniform inclined background field. Figure 2 shows the field in each of the simulations that we performed. The strong bipolar field near the surface creates a confining strapping field (cyan field lines) above the PIL beneath the separatrix of the 3D null (silver field lines). The field is constructed by superposing 16 vertically oriented sub-photospheric dipoles and the uniform background field,

$$\mathbf{B} = (c_1 \cos \theta, c_1 \sin \theta, 0) + \sum_{i=1,16} \nabla \times \mathbf{A}_i, \quad (1)$$

$$\mathbf{A}_i = \frac{b_i x_i^3}{2[x_i'^2 + (y_i' - y_c)^2 + z_i'^2]^{3/2}} \times [-z_i' \hat{\mathbf{y}} + (y_i' - y_c) \hat{\mathbf{z}}], \quad (2)$$

where $c_1 = -1.077$, θ is the angle of the field clockwise from the vertical, and $x_i' = x - x_i$, $y_i' = y - y_i$, and $z_i' = z - z_i$. The values for b_i , x_i , y_i , and z_i are given in Table 1. The photosphere is located at $x = 0$. In the three simulations, we set $\theta = -22^\circ$, 0° , and $+22^\circ$ (corresponding to Figures 2(a)–(c), respectively). The coordinate y_c determines the position along the y -axis where the bipolar region is situated; we used $y_c = -5.0$, -0.5 , and -5.0 for $\theta = -22^\circ$, 0° , and $+22^\circ$, respectively. The peak field strength in the parasitic polarity in each configuration is $B \approx 17$. The width of the separatrix dome at the photosphere varies from $w \approx 5$ at its narrowest to $w \approx 7$ at its widest, giving an average width of $w \approx 6$. The height of the null varies from $h \approx 1.7$ for $\theta = -22^\circ$ to $h \approx 2.0$ for $\theta = +22^\circ$.

For maximum generality, we solved the equations in nondimensional form. For purposes of direct comparison to

Table 1
Dipole Parameters

i	b_i	x_i	y_i	z_i
1	-6.0	-1.0	-0.5	-1.0
2	-6.0	-1.0	-0.5	-0.5
3	-6.0	-1.0	-0.5	-0.0
4	-6.0	-1.0	-0.5	-0.5
5	-6.0	-1.0	-0.5	-1.0
6	-6.0	-1.0	-0.0	-0.0
7	-6.0	-1.0	-0.0	-1.0
8	-6.0	-1.0	-0.0	-1.0
9	-5.3	-1.0	-1.5	-1.0
10	-5.3	-1.0	-1.5	-0.5
11	-5.3	-1.0	-1.5	-0.0
12	-5.3	-1.0	-1.5	-0.5
13	-5.3	-1.0	-1.5	-1.0
14	-5.3	-1.0	-1.0	-0.0
15	-5.3	-1.0	-1.0	-1.0
16	-5.3	-1.0	-1.0	-1.0

observations, we can introduce scaling factors typical of the corona. For the set of equations solved in the simulation (given below), fixing a typical length scale (L_s), plasma density (ρ_s), and magnetic field strength (B_s) is sufficient to fully define the scale values of other variables. We have

$$V_s = \frac{B_s}{\sqrt{\rho_s}}, \quad t_s = \frac{L_s}{V_s}, \quad (3)$$

$$E_s = B_s^2 L_s^3, \quad P_s = B_s^2, \quad (4)$$

where V_s scales the velocity, t_s the time, E_s the total energy, and P_s the pressure (and, subsequently, the temperature through the ideal gas law). Choosing $L_s = 4 \times 10^8$ cm, $B_s = 2$ G, and $\rho_s = 4 \times 10^{-16}$ g cm $^{-3}$ gives $V_s = 1000$ km s $^{-1}$, $t_s = 4$ s, $E_s = 2.56 \times 10^{26}$ erg, and $P_s = 4$ dyn cm $^{-2}$. The scaled average width of the separatrix dome in each case becomes $\bar{w} \approx 24$ Mm, and the scaled peak field strength within the parasitic polarity becomes $\bar{B} \approx 34$ G. In the results presented below, we use these scalings to convert our nondimensional numerical results to solar values. Note, however, that the quoted values can be modified by redefining any of our baseline scale parameters L_s , ρ_s , and B_s to apply the results to a particular observed jet.

The filament channel is created by prescribing a photospheric flow that follows the contours of B_x within the positive (parasitic) polarity patch of the large-scale bipole. The spatial dependence of the velocity pattern is calculated from (Wyper & DeVore 2016)

$$\mathbf{v}_\perp = v_0 g(B_x) \hat{\mathbf{x}} \times \nabla B_x, \quad (5)$$

$$g(B_x) = k_B \frac{B_r - B_l}{B_x} \tanh\left(k_B \frac{B_x - B_l}{B_r - B_l}\right), \quad B_l \leq B_x \leq B_r, \\ = 0, \text{ otherwise,} \quad (6)$$

where B_x is the spatially varying vertical field component and B_l , B_r , k_B , and v_0 are fixed constants set to 0.8, 15.0, 4.0, and 1.0×10^{-4} , respectively. Figure 2(d) shows the driving flow for $\theta = +22^\circ$ (the photospheric field distribution and hence the velocity profile vary little about $y = y_c$ among the three experiments). The high gradient in B_x across the PIL at the

center of the bipole generates the fastest flows at this location (purple strip on the right-hand side) and helps to form the filament channel there. The driving is reduced to zero a small distance from the center of the positive polarity to minimize the perturbation applied to the inner spine of the null. The peak driving speed for this velocity profile is $v_\perp \approx 0.03$ (30 km s $^{-1}$), which is subsonic and highly sub-Alfvénic (discussed below), so that the field in the volume evolves quasi-statically as occurs in the corona.

The flow is ramped up smoothly, held constant for a time, and then reduced to zero before the onset of the jet in each simulation. This is a numerically convenient way in which to form the filament channel and inject magnetic free energy into the corona. The flow is subsonic and sub-Alfvénic, so the field evolution is quasi-static; however, for our coronal scalings it is still over an order of magnitude faster than typically observed surface flows on the Sun. Therefore, we reduced the flow speed to zero well before jet onset in each simulation, to avoid any direct driving of the jet by the imposed flow. This separates completely the artificially fast energy injection process from the dynamically self-consistent mini-filament eruption and reconnection-driven jet onset that occur later. The length of the constant driving phase was varied between each run, such that for $\theta = +22^\circ$, 0° , and -22° the total driving time was $t_d = 300$ (20 minutes), 350 (23 minutes 20 s), and 450 (30 minutes), respectively. Different driving periods were required as a result of the high sensitivity of the breakout reconnection to the background-field inclination angle. This is discussed further in Section 5.2. Each simulation was halted before the jet disturbance reached the top boundary of the domain.

We use the Adaptively Refined Magnetohydrodynamics Solver (ARMS; DeVore & Antiochos 2008) to solve the ideal MHD equations in the form

$$\frac{\partial \rho}{\partial t} + \nabla \cdot (\rho \mathbf{v}) = 0, \quad (7)$$

$$\frac{\partial (\rho \mathbf{v})}{\partial t} + \nabla \cdot (\rho \mathbf{v} \mathbf{v}) + \nabla P - \frac{1}{\mu_0} (\nabla \times \mathbf{B}) \times \mathbf{B} = 0, \quad (8)$$

$$\frac{\partial U}{\partial t} + \nabla \cdot (U \mathbf{v}) + P \nabla \cdot \mathbf{v} = 0, \quad (9)$$

$$\frac{\partial \mathbf{B}}{\partial t} - \nabla \times (\mathbf{v} \times \mathbf{B}) = 0, \quad (10)$$

where t is the time, ρ is the mass density, $P = \rho RT$ is the thermal pressure, $U = P/(\gamma - 1)$ is the internal energy density, $\mu_0 = 4\pi$ is the magnetic permeability, and \mathbf{B} and \mathbf{v} are the 3D magnetic and velocity fields, respectively. An ideal gas is assumed with ratio of specific heats $\gamma = 5/3$. We use a uniform plasma density, temperature, and pressure of 1.0, 1.0, and 0.01, respectively, so the nondimensional gas constant is $R = 0.01$. With coronal scalings the density and temperature are 4×10^{-16} g cm $^{-3}$ and 1.2×10^6 K, respectively. The corresponding plasma $\beta \approx 0.22$ in the background field and drops to $\beta \approx 8.8 \times 10^{-4}$ at the surface within the parasitic polarity. The initially uniform sound speed $v_s \approx 0.13$ (130 km s $^{-1}$), while the Alfvén speed varies from $v_a \approx 0.3$ (300 km s $^{-1}$) in the background field to $v_a \approx 4.85$ (4850 km s $^{-1}$) in the parasitic polarity. We used box sizes of $[0, 120] \times [-20, 100] \times [-20, 20]$, $[0, 160] \times [-20, 20] \times [-20, 20]$, and $[0, 160] \times [-100, 20] \times [-20, 20]$ for the

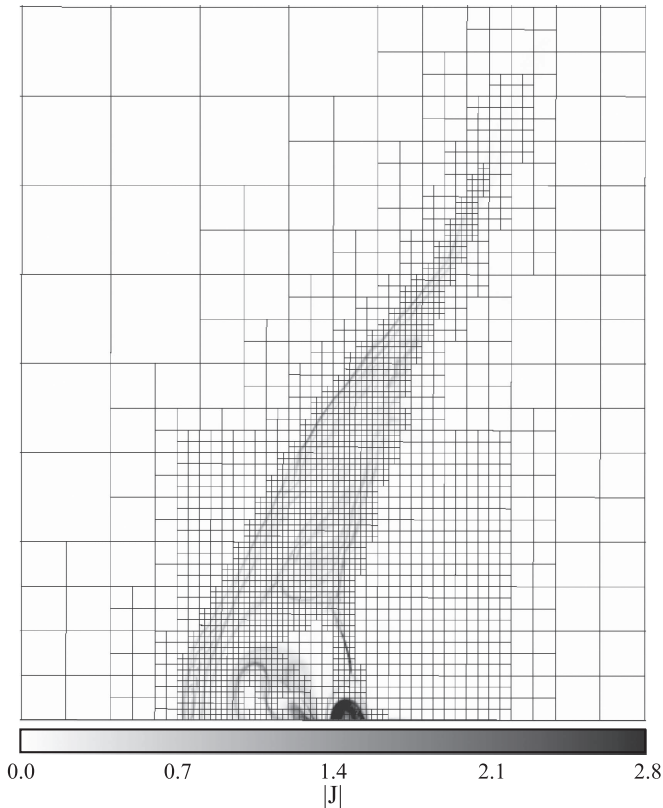


Figure 3. Adaptively refined grid during the jet at $t = 31$ minutes 20 s in the $\theta = +22^\circ$ simulation. Shown are cross sections of the grid blocks in the $z = 0$ plane. Each block contains $8 \times 8 \times 8$ cells. The shading corresponds to nondimensional electric current density ($\times 1.5 \times 10^{-3} \text{ A m}^{-2}$ with coronal scalings).

simulations with $\theta = +22^\circ$, 0° , and -22° , respectively. Open, zero-gradient boundary conditions were used on the top and side boundaries, whereas the bottom is closed and line-tied with zero tangential velocity everywhere except in the region of boundary driving. Reconnection occurs through numerical diffusion in the simulations. As we are primarily interested in the flow dynamics and the evolution of the magnetic field, we neglected gravity, the associated density and temperature stratification, and the thermodynamic effects of thermal conduction and radiative losses on the plasma. These simplifications mean that we cannot make meaningful predictions of the plasma radiation signatures in our simulated events; however, we expect that they would have little consequence for the magnetic- and flow-field evolution in our low- β system.

The adaptive mesh employed by ARMS is managed using the PARAMESH toolkit (MacNeice et al. 2000). The grid refines/de-refines according to local measures of the gradient and field strength of the magnetic field (see the Appendix of Karpen et al. 2012). Extra resolution is added where there are high gradients in the magnetic field, such as at current sheets and shocks, and, just as importantly, is removed in regions lacking such features. Figure 3 shows the block-adapted grid in the simulation with $\theta = +22^\circ$ during the evolution of the jet. Fine-scale grid blocks (each containing $8 \times 8 \times 8$ cells) outline both the jet front and the current layers on the separatrix dome. In each simulation, the background grid consists of blocks at one level below the minimum refinement level shown in Figure 3. The grid was allowed to refine

dynamically up to five levels beyond this background. We imposed refinement to four levels above the background in a small region that completely envelopes the separatrix dome, and to the maximum of five levels in a thin layer that extends over the driving region at the surface. The adaptive-mesh capability of ARMS was crucial to resolving simultaneously the dynamics of the small-scale separatrix dome and those of the large-scale jet front.

3. Jet Mechanism

In each simulation, our system follows the same basic evolutionary sequence and exhibits four main phases: *filament channel formation*, *breakout*, *eruptive jet*, and *relaxation*. A schematic of the first three phases of this sequence is shown in Figure 4. The configuration consists of just two distinct flux systems, open and closed field, separated by a null point (NP; Figure 4(a)). Because the bipolar surface flux distribution is elongated in the out-of-plane direction of the figure, the evolution can be understood most easily by referring to the four-flux color scheme used in the figure: an internal closed-flux region that eventually hosts the filament (cyan field lines) is flanked by side lobes of both closed and open flux (green field lines) and is topped by oppositely directed open flux (red field lines) on the far side of the null. This setup is topologically identical to the configuration investigated by Lynch et al. (2008), who showed that it can give rise to large-scale breakout CMEs with eruptive flares. The main, but significant, difference is that in the setup for breakout CMEs studied by Lynch et al. the scale of the null separatrix is such that the ambient field strength declined with height above the photosphere. In addition, the external open-field region closed remotely back to the Sun. The role of the background field strength in suppressing or allowing ideal expansion during the evolution is the crucial factor that dictates the nature of the eruption (jet versus CME) in the two setups (Wyper et al. 2017).

As the footpoint driving shown in Figure 2(d) proceeds, the large shear flow near the center of the bipole forms a strongly magnetically sheared filament channel (yellow field lines) along and above the PIL (Figure 4(b)). The rising magnetic pressure within the closed-field region expands the filament channel preferentially. Due to the strong strapping field (cyan field lines) overhead, the expanding sheared field increasingly stretches out to develop a quite flat midsection above the PIL (see also Antiochos et al. 1994; DeVore & Antiochos 2000, 2008; Aulanier et al. 2002). Using 1D models with comprehensive descriptions of the thermodynamics, Karpen et al. (2001, 2005) have shown that such regions can host long-lived condensations that resemble cool, counterstreaming filament plasma (see also Luna et al. 2012). Over time, the null point above the strapping field becomes increasingly compressed, and a breakout current sheet (BCS; Figure 4(b)) forms there.

Eventually, reconnection sets in at this sheet, removing some of the strapping field above the filament channel by transferring flux to the closed field under the far side of the dome and to the open field exterior to the near side of the dome (green field lines; Figure 4(c)). The resultant upward lifting of the sheared field forms an initially weak current sheet (pink bar) below the filament. There are no null points within the channel, due to the strong out-of-plane field component. We infer from the presence of this current layer and the flux rope field lines that quasi-separatrix layers (Titov 2007) form around the filament and cross over beneath it (gray lines, Figure 4(c)) at a

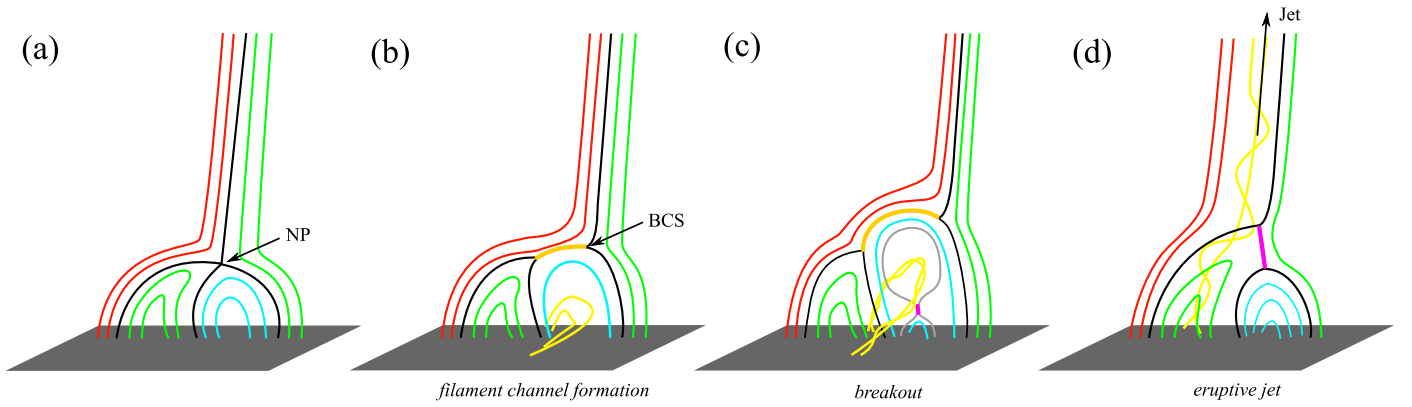


Figure 4. Schematic of the evolutionary sequence that produces breakout jets. Green field lines show both the open (right) and closed (left) side-lobe regions. Cyan field lines below the null point show the strapping field that holds down the yellow field lines of the sheared filament/flux rope. Red field lines show the overlying background (open) field. Black field lines show the separatrix and spines of the null point. Gray lines show the cross section of the quasi-separatrix layer (hyperbolic flux tube) around (below) the flux rope. NP = null point; BCS = breakout current sheet; FCS = flare current sheet.

hyperbolic flux tube (Titov et al. 2002). Slow reconnection occurs at their intersection, the weak current sheet, forming field lines that coil around the underside of the preexisting filament. The growing flux rope rises at a slowly increasing rate determined principally by the removal of strapping field at the overlying BCS. At some point, the positive feedback between the removal of the strapping field and the rise of the flux rope reaches a critical threshold, beyond which eruption is inevitable (Antiochos et al. 1999; Karpen et al. 2012; Wyper et al. 2017).

Upon reaching the breakout sheet, the flux rope begins to reconnect rapidly with the external open field. This launches nonlinear Alfvén waves that convect magnetic energy and compressed, accelerated plasma outward along the open field lines as the body of the jet (Figure 4(d)). In addition, this rapid opening of the flux rope induces explosive interchange reconnection within the flare current sheet (FCS) left in its wake, producing the jet bright point. Subsequently, after the jet front has propagated away along the open field, the flare reconnection subsides and the closed-field region relaxes toward a new equilibrium configuration resembling the potential field with which we started (Figure 4(a)).

4. Overview of Energies and Morphologies

The durations and onset times (vertical dotted lines) of the four evolutionary phases are indicated in Figure 5, where they are displayed along with the total free magnetic, kinetic, and injected energies. We calculated the energies from

$$E_{\text{mag}} = \iiint_V \frac{B^2}{8\pi} dV - \left[\iiint_V \frac{B^2}{8\pi} dV \right]_{t=0}, \quad (11)$$

$$E_{\text{kin}} = \iiint_V \frac{1}{2} \rho v^2 dV, \quad (12)$$

$$E_{\text{inj}} = \int \left[\iint_{x=0} \frac{1}{4\pi} (\mathbf{v} \cdot \mathbf{B}) B_x dS \right] dt. \quad (13)$$

Because the driving profile maintains the B_x distribution on the photosphere and the simulations were halted before the jet reached the top or side boundaries, the lowest-energy (potential) magnetic field remains the same throughout the evolution in each case. Thus, E_{mag} in Equation (11) represents the free energy stored within the magnetic field. E_{kin} is the equivalent for kinetic energy, since the plasma is initially at rest. E_{inj} is the cumulative

injected Poynting flux across the photosphere due to the boundary driving. Under an ideal, quasi-static evolution, E_{mag} should always equal E_{inj} (neglecting small effects due to plasma energy).

There are significant differences between durations of each phase among our simulations, but the qualitative changes in the energies are quite similar in all cases. The filament channel formation phase commences immediately, at $t = 0$, when the footpoint driving was turned on smoothly over a short ramp-up interval. Thereafter, the footpoint motion was held steady for some time and then turned off smoothly over a short ramp-down interval. Through experimentation, we found durations of steady motion that were sufficient in each case to generate an eruptive jet. The resulting driving profiles are the dashed curves shown in the figure. During this formation phase, E_{kin} is negligible and E_{inj} and E_{mag} follow each other closely. This indicates that the evolution remains quasi-static and quasi-ideal, and nearly all of the energy injected by the boundary driving is stored as free magnetic energy.

Some early reconnection and energy release occur in the simulations with $\theta = 0^\circ$ and -22° toward the end of this phase. In these cases the footpoint of the inner spine of the null falls within the patch of surface motions and so is displaced by the driving. This forms a current layer at the null point and drives reconnection that acts to add flux above the filament channel, further stabilizing it. Both simulations were deemed to have transitioned to the breakout phase when the expansion of the filament channel overcomes this initial reconnection, so that flux from above the filament starts to be removed in the manner of Figures 4(b)–(c). For $\theta = +22^\circ$ the inner spine is undriven and the breakout phase begins once the BCS forms at the null and reconnection begins.

Figures 6–8 show a side view of each of our configurations at three times (left to right) during their evolution. The left column shows each case at approximately the time of transition from the filament channel formation phase to the breakout phase. Field lines are traced from undriven line-tied footpoints on the photosphere and are colored the same as in our schematic diagram (Figure 4). Color shading in the $z = 0$ plane shows current-density magnitude. The fan planes have elongated upward substantially from the initial configurations shown in Figure 2 and are outlined by moderately strong currents (white shading). The filament channels host the strongest electric currents (red shading) and strongly sheared

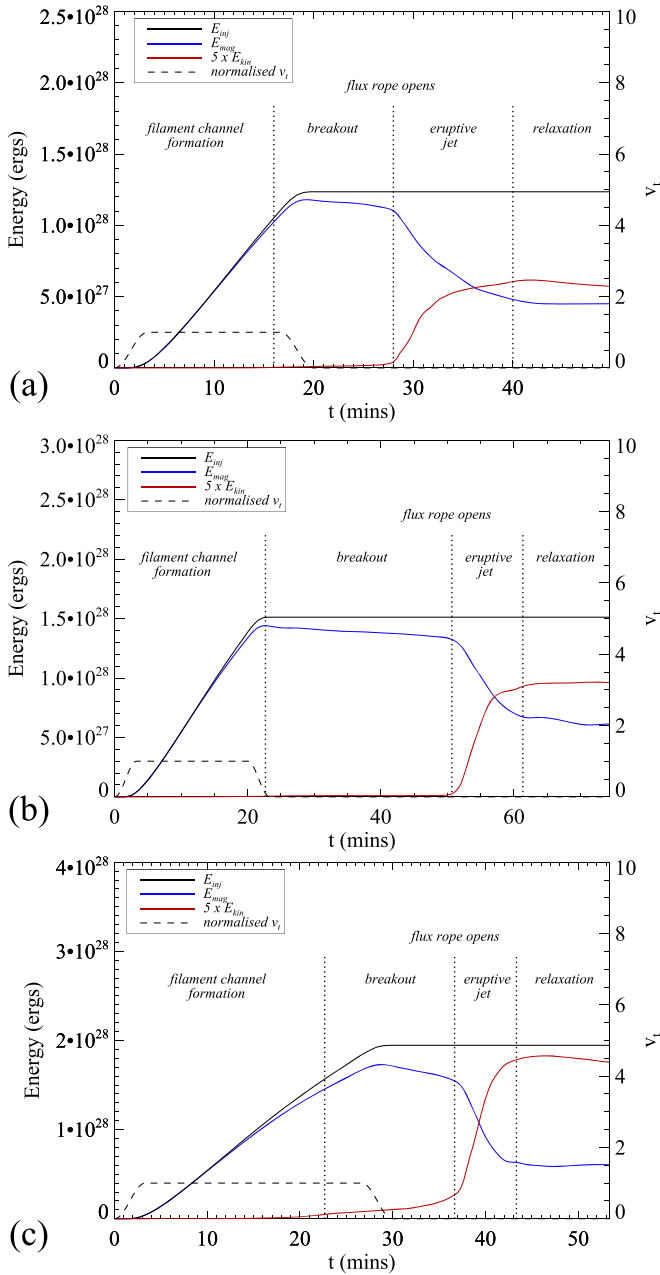


Figure 5. Changes in free magnetic (E_{mag} ; blue), kinetic (E_{kin} ; red), and injected (E_{inj} ; solid black) energies in each simulation. (a) $\theta = +22^\circ$; (b) $\theta = 0^\circ$; (c) $\theta = -22^\circ$. Dashed lines show the time dependence of the footpoint driving profile (v_t , normalized to unity). Note that different axes are used for energy and time in each plot and E_{kin} is multiplied by 5 for easier comparison.

magnetic fields (yellow field lines). The BCSs, above and left of the filament channel arcades of loops at the Y points of the external open field, have locally enhanced current densities.

As the breakout progresses, the filament channel fields slowly distend upward toward the breakout current layer. This is evident in the middle column of Figures 6–8, whose images are taken from about halfway through this phase. One key feature to note here is the change in the innermost flux from the left open regions (red field lines): it has reconnected, so that it now closes back to the Sun adjacent to the filament channel. This marks the progression of the breakout reconnection during this phase. The energy plot, Figure 5, shows that there is a gradually increasing deviation between E_{inj} and E_{mag} due to the

quasi-steady release of stored magnetic energy by this reconnection. The release is slow, as evidenced by the very small to negligible E_{kin} during this phase (notice that E_{kin} is multiplied by 5 to improve its visibility in the figure).

The transition from the breakout to the eruptive-jet phase occurs when the rising flux rope in the filament channel began to reconnect with the external open field across the BCS. This transition is an inherently 3D and very dynamic process. It is shown in Figure 9 for $\theta = +22^\circ$. The left panels show the current structures just prior to the flux rope opening. The BCS curves over the top of the rising flux rope, shown as a curved iso-surface of J . Beneath this a strong volumetric current outlines the shape of the flux rope and includes the current layer below the rope. The middle panels show a time soon afterward where the flux rope is beginning to open (yellow field lines). At this time, the BCS combines with the current layer beneath the flux rope, forming an extended current structure that wraps around the separatrix surface. As this occurs, the interchange reconnection region (effectively the null point, or cluster of null points, within the current structure) moves through the curved current structure from the top of the dome to behind the opening flux rope. This region becomes the explosively interchanging flare current sheet. The right panels show the flare current sheet once it is fully formed. The remnants of the BCS now form the filamentary current layers that separate the untwisting flux rope from the ambient field and propagate away with the jet.

The magnetic field and current-density structures at about the midpoint of the eruptive-jet phase are shown in the right columns of Figures 6–8. The initially fully open (red) flux has now almost completely closed down to the surface as a consequence of the breakout reconnection. In each case, a broad spire of intense, filamentary currents extends upward into the corona from the reconnected-flux region, bordered on the left of the image by a strip of strong current demarcating the remnants of the BCS. These currents are markers of the nonlinear Alfvén waves launched onto open field lines. Figure 10 shows the vertical (v_x ; top row) and out-of-plane horizontal (v_z ; bottom row) components of the supersonic plasma flow in the three cases (left to right). The vertical flow is generally outward over most of the jet volume. The horizontal flow, in contrast, reverses direction across the center of the jet body. This indicates a rotational or torsional motion of the plasma, as the magnetic twist transferred from closed to open field is carried away as an untwisting wave. The resulting helical motions closely resemble those observed in many solar jets.

As can be seen in Figure 5, concurrent with or very soon after this opening of the flux rope, there is a steep drop in E_{mag} and a simultaneous sharp increase in E_{kin} . These changes mark the sudden onset of the sustained, explosive interchange reconnection. The launching of the nonlinear Alfvén waves, together with the plasma acceleration within the flare current sheet, converts between 25% and 35% of the released free magnetic energy to kinetic energy of bulk flow in the jet, amounting to some 10^{28} erg. The associated durations of the eruptive-jet phase range from 6 to 12 minutes. These energies and durations are consistent with those observed in coronal jets (Shibata et al. 1992; Savcheva et al. 2007).

Late in the eruptive-jet phase, the jet front has propagated away from the separatrix dome and the explosive interchange

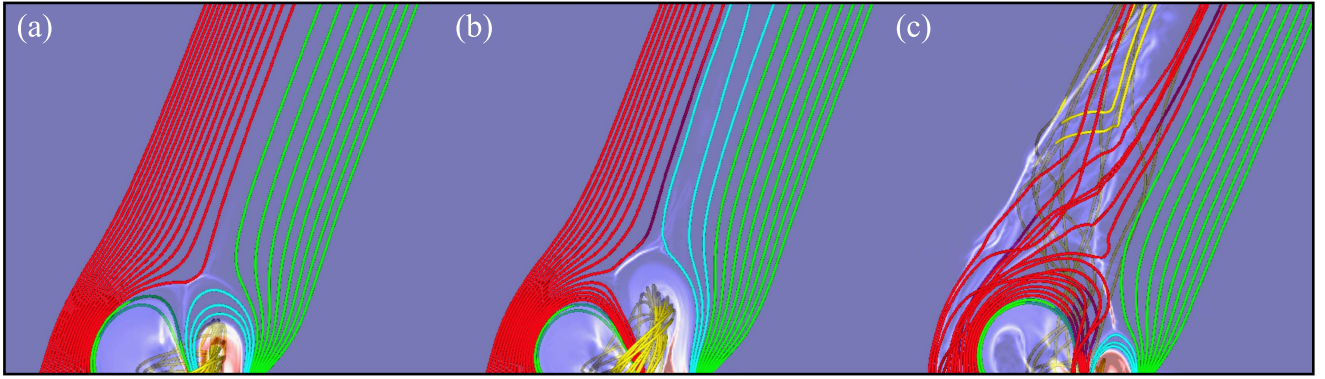


Figure 6. Eruption sequence when $\theta = +22^\circ$. (a) $t = 16$ minutes; (b) 24 minutes; (c) 31 minutes 20 s. Shading shows electric current density ($|J|$) with the same color scale as Figure 13. Red, cyan, and green field lines are traced from fixed, undriven footpoints along the y -axis ($z = 0$) on the photosphere. Yellow field lines that pass through the flux rope are traced from undriven photospheric footpoints.

(An animation of this figure is available.)

reconnection slows. The previously rapid changes in E_{mag} and E_{kin} tail off, as can be seen in Figure 5. Each jet then enters a relaxation phase, during which both the reduced free magnetic energy and increased kinetic energy remain at nearly constant values. The high efficiency of the jet-generating reconnection processes is indicated by the fact that more than 50% of the initially stored free magnetic energy has been liberated by the time of transition to the relaxation phase.

5. Detailed Comparison of Evolutionary Phases

5.1. Filament channel Formation

Since the filament forms deep within the closed-field region and away from the influence of the background-field inclination, the filament channel formation phase is similar in each simulation. However, when $\theta = -22^\circ$ and 0° , the onset of the breakout phase is delayed long enough (see below) that the highly sheared field within the filament channel is converted to a flux rope by so-called “tether-cutting” reconnection (Moore & Roumeliotis 1992; Moore et al. 2001); see Figures 11(b) and (c). This connectivity change is induced within a narrow vertical current layer that forms along the PIL as the field there is sheared. The reconnection lengthens the higher sheared field lines, while also adding twist to form a flux rope. Additionally, less sheared field lines are formed beneath the rope (Figure 11, pink field lines; see van Ballegoijen & Martens 1989). This slow reconfiguration of the field releases negligible amounts of free energy (Figure 5) and leads to no rapid dynamics. These flux ropes are actually remarkably robust, and in test simulations where the driving was halted after the flux ropes form, but prior to the onset of the breakout phase, the system would find a new equilibrium with the flux rope embedded in the closed-field region. These results tell us three important things: (1) tether-cutting reconnection is not the driver of these jets, (2) ideal instabilities of the flux rope, such as kink or torus, are also not the drivers, and (3) the subsequent breakout behavior is not sensitive to whether a sheared arcade or true flux rope is present initially.

5.2. Breakout

The inclination angle of the field plays an important role in the formation of the BCS and, subsequently, in the onset of the eruptive jet. For large positive values of θ , the background field is in the opposite direction to the horizontal field of the

compact bipole. Consequently, the null point is positioned more or less directly above the parasitic polarity of the bipole (Figure 2(a)). The expanding strapping field pushing up into the oppositely directed background field then readily forms the BCS there. This explains both the early onset and the comparatively short duration of the breakout phase for the case $\theta = +22^\circ$ (Figure 5, top).

As θ is reduced and the background-field orientation rotates to vertical and beyond, the null point moves farther from the PIL of the bipole. This shifts the photospheric footpoint of the inner spine of the null farther away from the PIL and increases the amount of strapping field above the PIL where the filament channel will form (Figure 2(c)). As the null is positioned farther to the side, the upward expansion of the strapping field above the filament channel less readily pushes into the null and the BCS is formed later. This is compounded in our simulations by the rotational driving profile that shears the field on both sides of the dome, so that the dome as a whole expands upward. Thus, as the inclination angle changes, the effect on the null point changes from mainly compression across the fan plane (from pushing into the overlying field) with fast breakout sheet formation to mainly stretching along the fan plane (from mismatched expansion of the dome) with slow breakout sheet formation. In our tests, we found that driving the configuration with $\theta = 0^\circ$ for the same duration as $\theta = +22^\circ$ was insufficient to initiate strong breakout reconnection; instead, the system reached a new equilibrium. Clearly, a critical threshold of breakout reconnection must be achieved to initiate a jet, just as occurs in CME calculations (e.g., Karpen et al. 2012). The threshold would appear to be related to the balance of forces within the closed-field region. The breakout phase for $\theta = 0^\circ$ was almost twice as long as that for $\theta = +22^\circ$ (Figure 5). This is primarily due to the additional strapping field that must reconnect across the BCS for $\theta = 0^\circ$.

One further consequence of the shift of the null position is that as θ is reduced and the footpoint of the inner spine migrates away from the PIL, it moves farther into the driving region. In our configurations, the inner spine was driven not at all for $\theta = +22^\circ$, only slightly for $\theta = 0^\circ$, but quite strongly for $\theta = -22^\circ$. Driving the spine concentrates the shear at the null, directly forming a near singularity in the current (Pontin et al. 2007; Wyper & Pontin 2014a) rather than the broad breakout sheet formed by the expansion of the field from below. The resultant boundary-driven reconnection adds an

additional strapping field above the filament channel and consequently has a further stabilizing influence. This effect dominates the early stages of the $\theta = -22^\circ$ evolution, which, together with the extra strapping field and positioning of the null away from the PIL, required significantly more driving to initiate the breakout process (Figure 5, bottom). Tests with shorter driving durations all reached new equilibria following an interval of reconnection at the null. By the time the breakout phase started, most of the flux beneath the dome had become strapping field above a large filament channel region (Figure 8(a)). Despite this, the ensuing breakout phase is shorter for $\theta = -22^\circ$ than for $\theta = 0^\circ$. This is a result of the intense breakout reconnection facilitated by the strong BCS in this case.

Figure 12 (top row) shows isosurfaces of mass density depicting the compressed exhaust plasma of the BCS in each jet. For $\theta = +22^\circ$, the outflows form a tapered spire (Figure 12(a)) that waves and undulates (see the online movie). This wave motion follows the onset of tearing in the breakout sheet, in which blobs of high-density plasma associated with small flux ropes are formed in and ejected from the sheet (Wyper & Pontin 2014b; Wyper et al. 2016). Plasma in the spire is ejected at around 150 km s^{-1} , only marginally above the background sound speed of 130 km s^{-1} . The strongest, nearly Alfvénic flows are concentrated downward over the surface of the separatrix. For $\theta = -22^\circ$, the spire is less coherent and more fragmented (Figure 12(c)). The outflows have a speed near the local Alfvén speed, $\approx 300 \text{ km s}^{-1}$. For $\theta = 0^\circ$, little density enhancement occurs as these outflows too are directed over the separatrix surface. A thin, transient spire is visible in Figure 12(b). These results suggest that regions of the corona with highly inclined open fields should exhibit outflows from the breakout reconnection that are visible as straight jetlike spires. In nearly vertical fields, on the other hand, the jet spire should be weak or even unobservable during the breakout phase.

5.3. Eruptive Jet

In each of our configurations, a violent change in behavior occurs when the flux rope reaches the BCS. Interchange reconnection opens the end of the flux rope previously rooted in the parasitic (positive) polarity of the bipolar region (yellow field lines in Figures 6–8, right panels). This launches a nonlinear torsional Alfvén wave as part of the twist within the flux rope propagates outward along the reconfigured open field lines in the manner first envisaged by Shibata & Uchida (1986). Plasma around the periphery of the unwinding flux rope is driven upward in a spiral with strong out-of-plane and upward components (Figure 10). However, the untwisting wave is only one aspect of each jet. The shift of the interchange reconnection site (described in Section 4) initiates explosive flare reconnection in the current sheet behind the rope. The reconnection accelerates plasma upward into the underside of the untwisting wave front and downward into low-lying flare loops. This bidirectional outflow is clear on the right side of the top panels in Figure 10. Note that like the BCS, the flare current sheet is fragmented, which creates substructure in v_x within the sheet. The sheet strengthens and reconnects explosively as the flux transferred from above the bipole to the other side of the dome slams back into the ambient field in the wake of the flux rope ejection (red field lines in Figures 6–8, right panels).

Figure 12 (bottom row) shows the untwisting jets that are formed. The kinked field lines (predominantly red) show part of the torsional wave launched by the opening of the flux rope. Isosurfaces of density highlight the compressed plasma that forms part of the jet outflow. The kinked field lines and density enhancements appear together but gradually separate as the two propagate outward (seen clearly in the online movies), with the torsional wave front traveling at the local Alfvén speed ($\approx 300 \text{ km s}^{-1}$) and the density enhancement closer to the local sound speed ($\approx 130 \text{ km s}^{-1}$). Pariat et al. (2016) recently described a very similar behavior in their coronal-jet simulations, attributing the formation of the slower density enhancement to plasma accelerated by the passage of the Alfvén wave. It seems likely that the same scenario is occurring here.

The sharp decrease in magnetic energy and increase in kinetic energy vary across the three configurations (Figure 5). For $\theta = +22^\circ$, the drop in magnetic energy begins steeply and progressively tails off as the jet proceeds over a duration of ≈ 12 minutes. As θ increases, the energy release interval shortens slightly to ≈ 10 minutes 40 s for $\theta = 0^\circ$ and then more dramatically to ≈ 6 minutes 40 s for $\theta = -22^\circ$. Correspondingly, the fraction of the free energy that is converted to kinetic energy increases from $\approx 25\%$ for $\theta = +22^\circ$ to $\approx 35\%$ for $\theta = -22^\circ$. The shortening of the jet period and increase in kinetic-energy conversion can be understood by considering where the magnetic energy is stored and released in each configuration. The free energy is injected as shear into the closed field, with the majority being found in the filament channel. For $\theta = 0^\circ$ and -22° , weak tether-cutting reconnection creates a flux rope from the highly sheared field within the channel, transferring shear from the low-lying field above the filament channel to the developing flux rope. This creates longer flux rope field lines and shorter reconnected loops beneath. An increasing fraction of the free energy stored in the closed field resides within the flux rope. Once the flux rope begins to erupt, additional tether-cutting reconnection lengthens it so that it extends farther around the circular PIL and receives more of the free energy stored within the structure. Thus, the increasing duration of driving for the simulations with progressively smaller θ stores more free energy within the flux rope. The more impulsive energy release for smaller values of θ follows from a greater proportion of the stored free energy in the closed-field region being released promptly as the flux rope opens. The increased fraction of the free energy being converted to bulk kinetic energy then can be understood as resulting from a greater direct ideal acceleration of plasma by the untwisting torsional wave front.

5.4. Relaxation

Figure 13 shows the field configurations near the bipole in the aftermath of the jets. In each case, the null dome resets to a configuration similar to the initial condition, but with a slowly reconnecting current layer at the null point. Some magnetic shear also remains in the closed-field region (particularly within the filament channel), as shown by the contours of strong volumetric current (white and red shading). Only a fraction of the shear on any given closed field line is released to propagate away when it is interchange-reconnected (e.g., Wyper et al. 2016). The remnant sheared field contributes the majority of the free magnetic energy at the end of the simulations (Figure 5). The interchange reconnection at the null continues to progressively tail off as the closed-field region relaxes

toward a new equilibrium. In each jet, the interchange reconnection continued until the simulation was halted, so that the jet front did not reach the top boundary. The free energy released during this relaxation phase was negligible.

6. Coronal Energy Injection

Once the jet is launched, it propagates upward along the ambient field, transporting energy (and also helicity) higher into the corona. To understand the details of this process, we calculated the cumulative energy transfer due to the Poynting and kinetic-energy fluxes across several different heights in each simulation. Specifically, we calculated

$$P(h) = \int \left[\iint_{x=h} \frac{1}{4\pi} [(\mathbf{v} \cdot \mathbf{B})B_x - B^2 v_x] dS \right] dt, \quad (14)$$

$$K(h) = \int \left[\iint_{x=h} \frac{\rho v^2}{2} v_x dS \right] dt, \quad (15)$$

where P is the cumulative Poynting flux, K is the cumulative kinetic-energy flux, and h is the height above the surface. The first term of P is the contribution from motions tangential to the surface (the shear component), while the second corresponds to contributions from emergence/submergence of the magnetic field (the vertical component). The results are shown in Figure 14.

The cumulative Poynting flux during the breakout phase behaves differently in each case. For $\theta = +22^\circ$ the Poynting flux is negative, for $\theta = 0^\circ$ it is essentially zero, and for $\theta = -22^\circ$ it is positive. During the breakout phase, both v_x and v_z are small at all of these heights above the surface, and the dominant contribution to the Poynting flux is from the $v_y B_y$ term directed perpendicular to the PIL of the bipolar region. (In contrast, the dominant contribution at the surface $h = 0$ is from the $v_z B_z$ shear term, which generates most of the injected energy E_{inj} discussed in Section 4). As the breakout reconnection proceeds, the open field in each configuration moves in the positive y direction (from left to right in Figures 6–8, for example) as it approaches the BCS, reconnects through the sheet, and then departs the sheet along with the reconnection exhaust. This produces a negative Poynting flux for $\theta = +22^\circ$ ($B_y < 0$), a negligible net flux for $\theta = 0^\circ$ ($B_y = 0$), and a positive Poynting flux for $\theta = -22^\circ$ ($B_y > 0$). These results imply that the energy in the overlying magnetic field directly above the bipole decreases, remains about the same, and increases, respectively, in the three configurations.

In all cases, once the jet is launched, a strong positive Poynting flux dominates as the torsional Alfvén wave propagates upward into the domain. The curves at greater heights rise progressively later owing to the time required for the wave to propagate to those higher altitudes. These impulsive increases are much larger in amplitude than the quasi-steady changes that occurred during the breakout phase.

In contrast to the Poynting flux, the kinetic-energy flux is always negligible during the breakout phase and then increases impulsively once the jet is launched. Unlike P , the curves for K at progressively greater heights do not decrease monotonically with height. At 266.7 Mm for $\theta = 0^\circ$ (Figure 14(e)) and 213.3 Mm for $\theta = -22^\circ$ (Figure 14(f)), for example, the kinetic-energy fluxes are slightly larger than those at the next lower height. This suggests that further conversion of free magnetic energy to kinetic energy is occurring within the

propagating jet front. Comparing the magnitudes of K and P , it is clear that the energy transfer is dominated by the Poynting flux. Although there is a significant upward acceleration of plasma in each jet (Figure 12), most of the kinetic energy resides within the rotational velocity component of the torsional Alfvén wave.

For completeness, we also calculated the cumulative enthalpy flux in each jet. Like the kinetic-energy flux, we found the enthalpy flux to be significantly smaller than the Poynting flux. Our results imply that the energy injected into the solar wind by coronal jets is far larger than what would be inferred from observations of only the jet plasma.

7. Discussion

7.1. Comparison to Observations

The jets produced by our model closely match several aspects of coronal jets involving mini-filaments. Jet mini-filaments are typically close in size to the width of the jet base, usually assumed to correspond to the closed-field region. Consequently, the lengths of mini-filaments vary with jet size, with quoted values varying from $l \approx 6$ Mm to $l \approx 36$ Mm (e.g., Sterling et al. 2015; Panesar et al. 2016). In our simulations, the sheared filament channel is of comparable size to the extent of the separatrix in the z direction. With our chosen scale values this is $l = 28$ Mm, falling within the range of observed values. Our filament channel also forms along the PIL of the strong preexisting bipolar field, as is observed (e.g., Adams et al. 2014; Panesar et al. 2016). Due to the highly simplified atmosphere and energy equation that we adopted, the cool, dense material associated with solar mini-filaments is not present in our simulations. However, the strongly sheared magnetic structure of the filament channel is replicated by our model.

The eruption sequence exhibited by our simulated jets matches well with numerous observations. For the three cases that we studied, we found that the intensity of the pre-jet breakout reconnection depends on the inclination of the ambient magnetic field: faster, denser outflows result when the field is highly inclined, whereas weaker outflows with less density contrast occur when the field is vertical. Some examples of blowout jets preceded by a tapered, inverted-Y-shaped jet have been reported (e.g., Liu et al. 2011; Hong et al. 2016; Zhang et al. 2016). The perspective makes it difficult to discern the inclination of the ambient field in the jet described by Hong et al. (2016). In the jets discussed by Liu et al. (2011) and Zhang et al. (2016), on the other hand, the ambient field is highly inclined, which is consistent with our findings. A clear example of a mini-filament jet in a nearly vertical field was described by Moore et al. (2015) and revisited in Wyper et al. (2017). A weak spire connects to the edge of a sharp interface between closed and open field, consistent with a weak tapered outflow from a BCS (forming the sharp interface) as seen in our jet experiment with $\theta = 0^\circ$ (e.g., Figure 7(b)).

The jets are produced in our model by a combination of an untwisting flux rope and plasma accelerated by the flare reconnection that occurs below. The broad, untwisting jet spire is consistent with many blowout jets. So too is the formation of flare loops by magnetic reconnection across our low-lying, vertical flare current sheet. With full plasma thermodynamics included, these loops should be heated by the reconnection process and, thus, correspond to the jet bright points formed

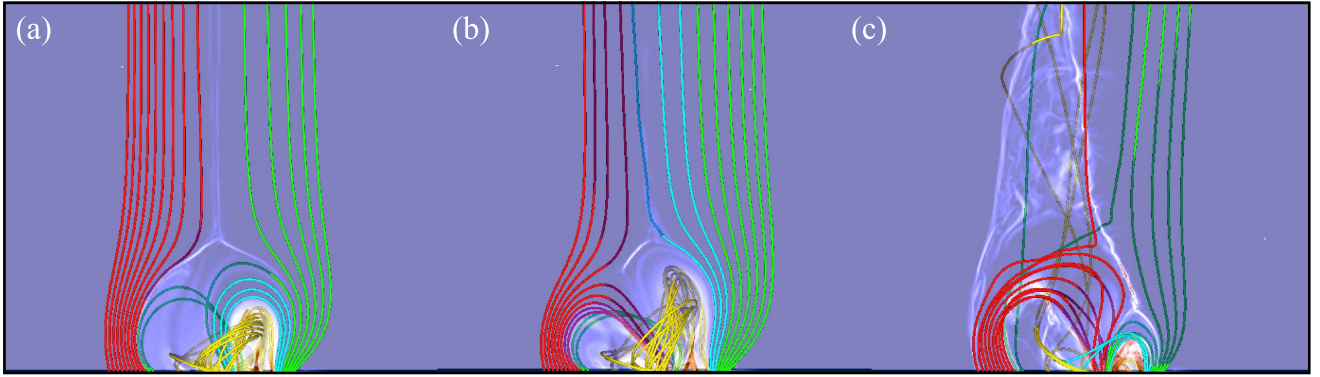


Figure 7. Eruption sequence when $\theta = 0^\circ$. (a) $t = 22$ minutes 40 s; (b) 45 minutes 20 s; (c) 54 minutes 40 s. Shading and field lines as in Figure 6. (An animation of this figure is available.)

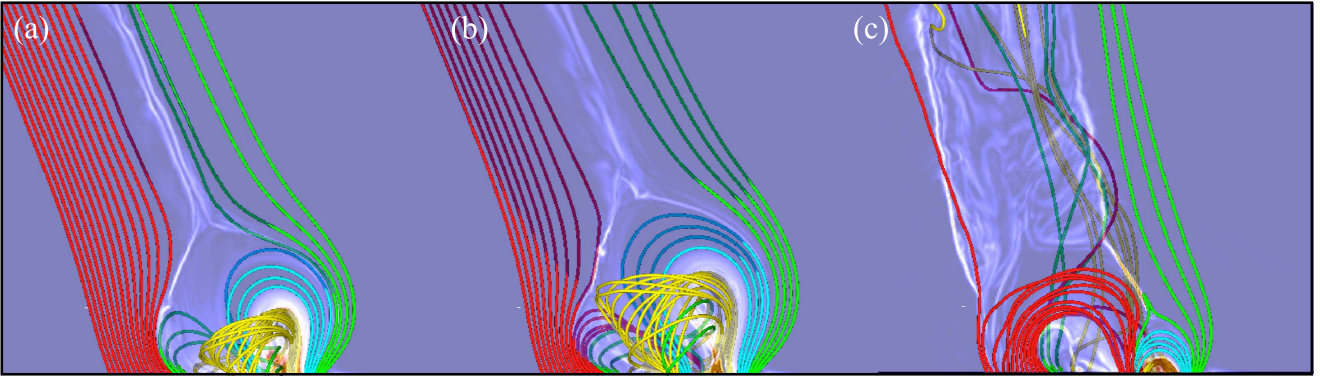


Figure 8. Eruption sequence when $\theta = -22^\circ$. (a) $t = 23$ minutes 20 s; (b) 30 minutes 40 s; (c) 40 minutes. Shading and field lines as in Figure 6. (An animation of this figure is available.)

beneath the erupting mini-filaments in the observations (e.g., Sterling et al. 2015). Our jet plasma is a combination of ambient material within the flux rope and material that has been processed by the flare interchange reconnection. This is consistent with the observed multithermal nature of many mini-filament jets (e.g., Adams et al. 2014; Sterling et al. 2015), which appear to be composed of both cool filament plasma and hot coronal plasma from the reconnection region. Our post-jet relaxation phase, during which the flare reconnection tapers off while producing a continued stream of plasma in the wake of the main jet, also seems to be a common feature of mini-filament jets (e.g., Liu et al. 2011).

Our simulations do not include all of the physics necessary to produce chromospheric/photospheric brightening (e.g., thermal conduction, radiation, and possibly nonthermal particles). Nevertheless, based on the magnetic field evolution in our jet model, we can make informed conjectures about the expected photospheric signatures. Spreading flare ribbons, similar in nature to those in large-scale two-ribbon flares, can be expected to form at the base of the new loops formed by the flare reconnection as the jet is launched. In addition, the intense interchange reconnection initiated as the flux rope reaches the BCS should create brightening around the base of the separatrix surface. The location of this brightening will shift as the interchange reconnection changes the footprint of the separatrix surface. Depending on the nearby distribution of flux, this brightening could be quasi-circular, as in some large-scale solar flares (e.g., Masson et al. 2012), or take the form of discrete patches, if the separatrix field predominantly connects to discrete

sources. Zhang et al. (2016) observed both the spreading small-scale flare ribbons and a larger-scale, quasi-circular, enclosing ribbon as the jet was launched. Hong et al. (2016) described a mini-filament jet in which the separatrix brightening occurred across several nearby discrete patches associated with discrete photospheric flux regions. Therefore, our jet model is also qualitatively consistent with these observations. However, to understand the nature and timing of the photospheric brightening in our model requires a detailed analysis of the changing magnetic topology. This task is left to future work.

Finally, as the jet front propagated outward in our simulations, we observed a separation of the strong magnetic field perturbation from the bulk plasma flow. The former propagated at the local Alfvén speed, while the latter traveled at close to the local sound speed. Similar simulation results have been reported by Pariat et al. (2016). Although we have not studied these features in any detail, we note that such a separation also has been reported for many observed jets (Cirtain et al. 2007; Savcheva et al. 2007).

7.2. Comparison to Previous Models

From our numerical experiments, we identified the breakout reconnection process as the dominant mechanism underlying the eruptive jet. In the picture presented, this reconnection initially is quasi-steady, creating a tapered outflow of plasma as envisaged originally by Shibata et al. (1992). Eventually, the reconnection transitions to an explosive phase as the rising flux rope encounters the BCS and opens up. The resulting

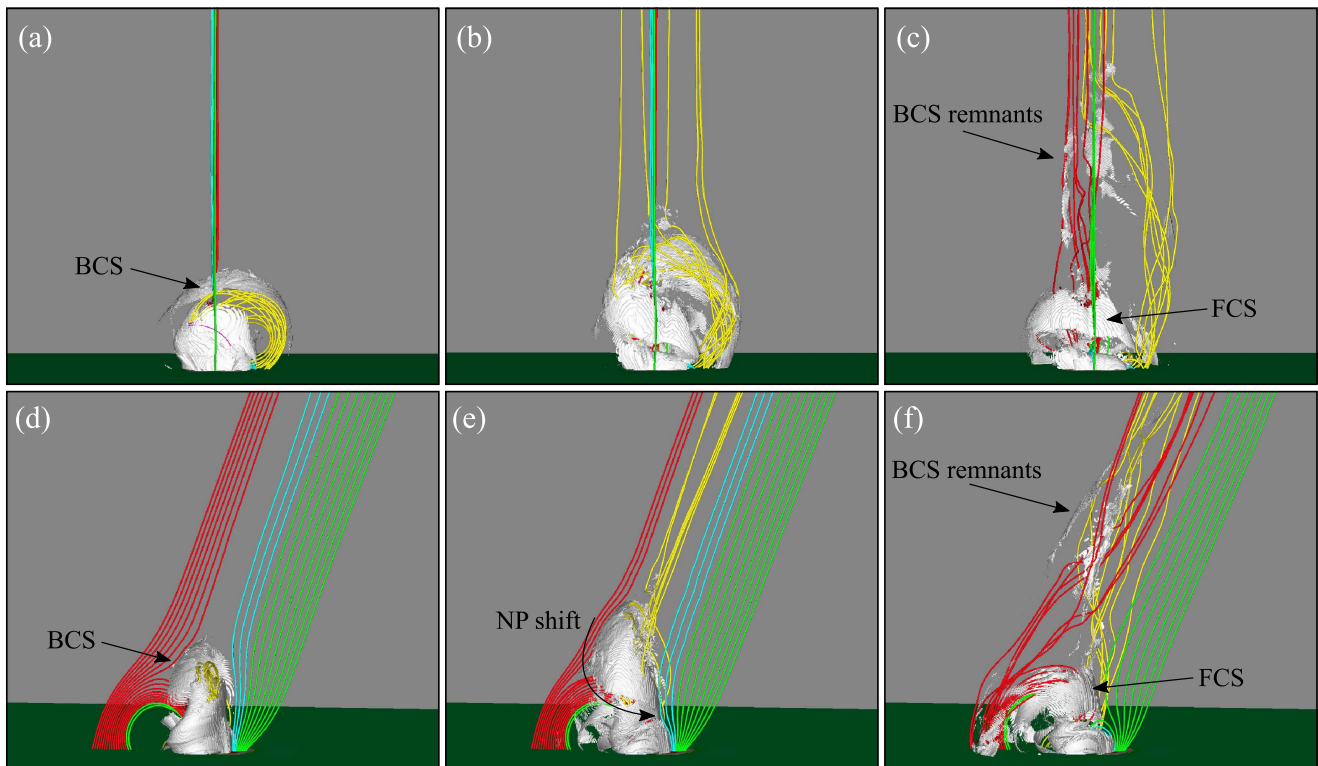


Figure 9. End-on (top row) and side (bottom row) views of the shift of the interchanging current layer as the flux rope opens for $\theta = +22^\circ$. White isosurfaces show $|J| = 1.0$ ($\times 1.5 \times 10^{-3} \text{ A m}^{-2}$ with coronal scalings). Field lines as in Figure 6. Left column: $t = 27$ minutes 20 s; middle column: $t = 29$ minutes 20 s; right column: $t = 31$ minutes 20 s. BCS = breakout current sheet; FCS = flare current sheet; NP = null point.

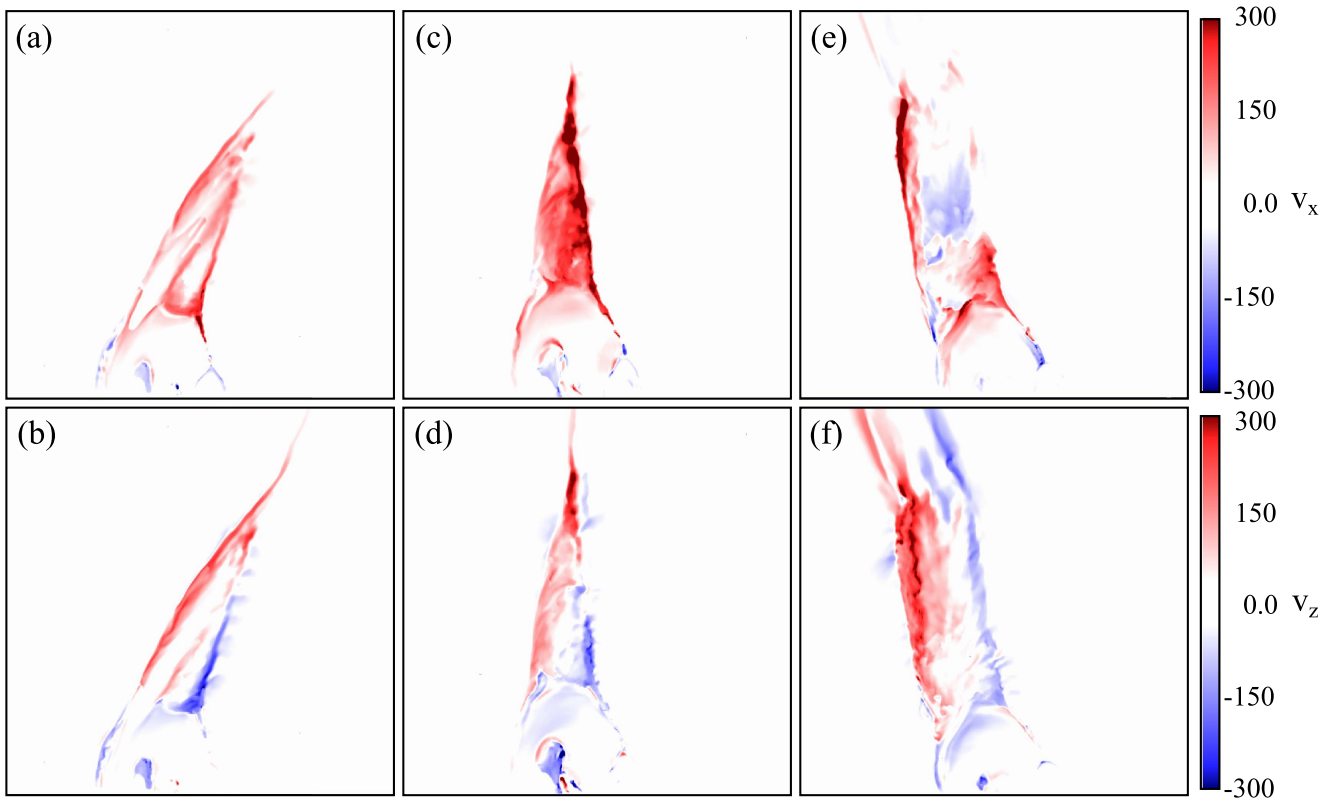


Figure 10. v_x (top) and v_z (bottom) in the $z = 0$ plane as the jet is launched. Left column: $\theta = +22^\circ$, $t = 31$ minutes 20 s; middle column: $\theta = 0^\circ$, $t = 54$ minutes 20 s; right column: $\theta = -22^\circ$, $t = 40$ minutes. All velocities are in km s^{-1} .

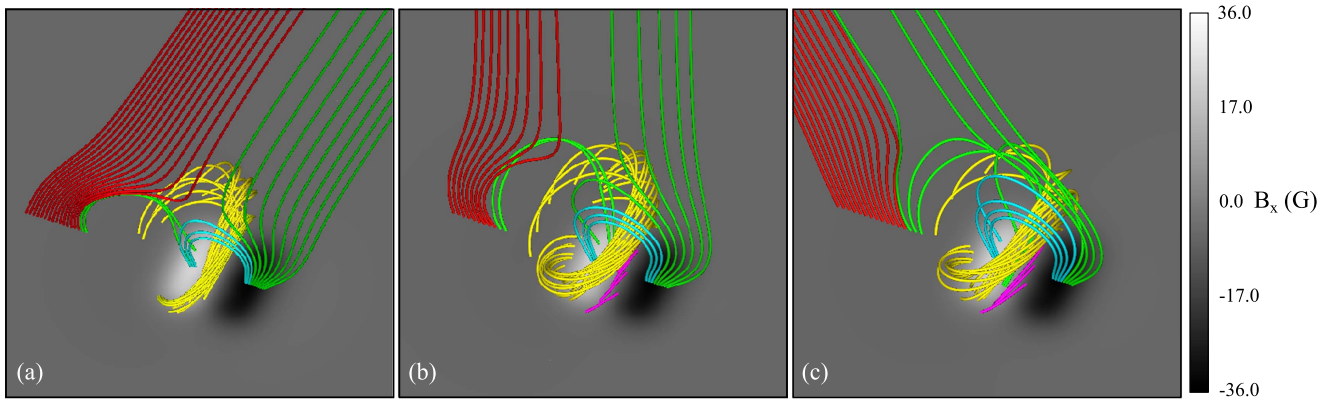


Figure 11. Filament channel field (yellow magnetic field lines). Bottom plane is color-shaded according to B_x . (a) $\theta = +22^\circ$, $t = 16$ minutes; (b) $\theta = 0^\circ$, $t = 22$ minutes 40 s; (c) $\theta = -22^\circ$, $t = 21$ minutes 20 s. In panels (b) and (c) shown in pink are the short, reduced shear field lines that form as the sheared arcade is converted to a flux rope by reconnection near the PIL.

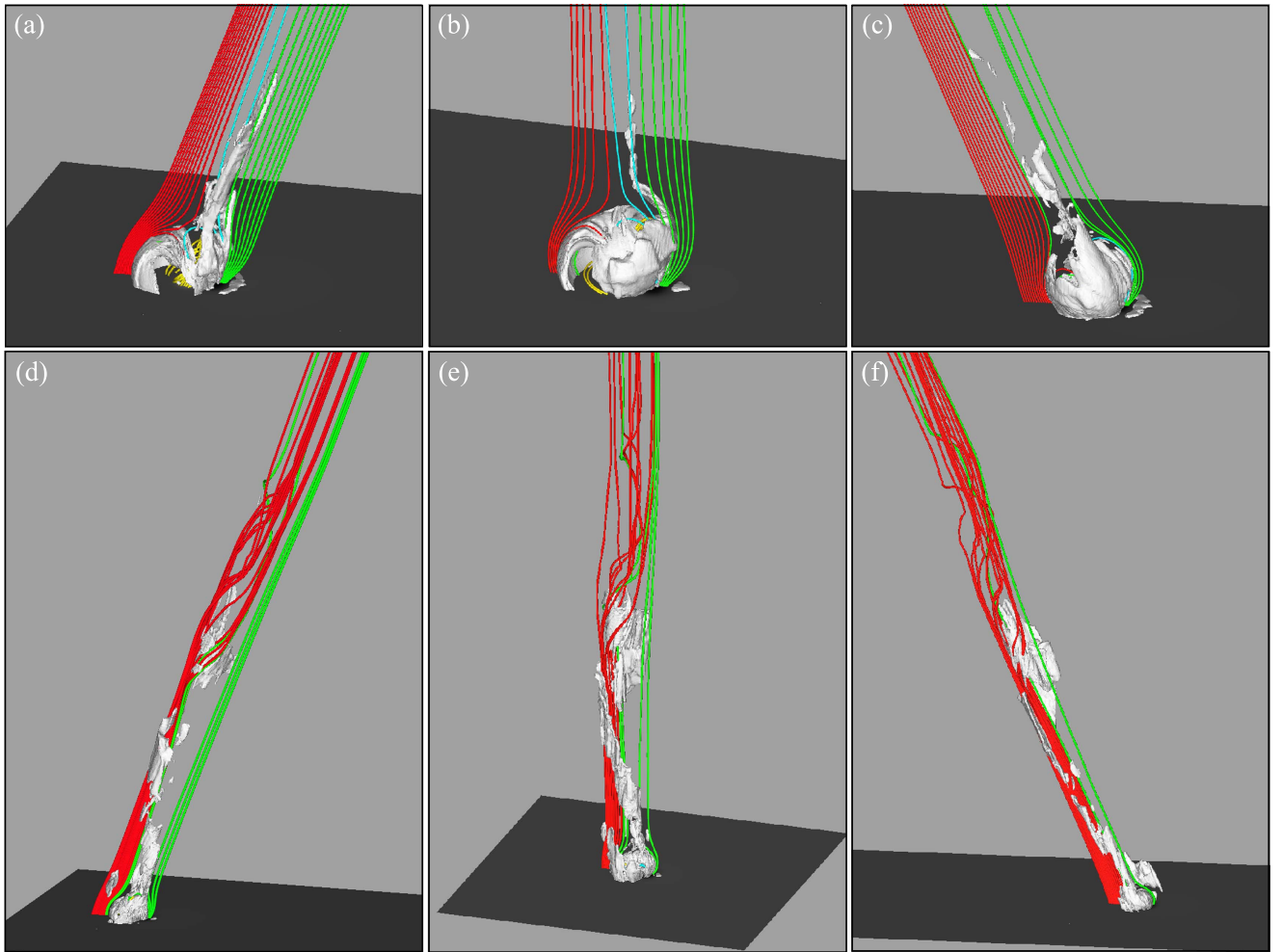


Figure 12. Morphology of the jet in each simulation. Top row: during the breakout phase. Bottom row: during the eruptive-jet phase. Bottom plane is color-shaded according to B_x as in Figure 11. Isosurfaces show mass density $\rho = 1.1$ ($4.4 \times 10^{-16} \text{ g cm}^{-3}$). (a) and (d): $\theta = +22^\circ$, $t = 22$ minutes 40 s and $t = 42$ minutes; (b) and (e): $\theta = 0^\circ$, $t = 40$ minutes 40 s and $t = 61$ minutes 20 s; (c) and (f): $\theta = -22^\circ$, $t = 24$ minutes and $t = 53$ minutes 20 s. The separation of the leading fast nonlinear Alfvén wave (indicated by the kinking of the open-field lines) from the trailing slower plasma outflow (depicted by the density isosurfaces) is evident during each jet. (An animation of this figure is available.)

untwisting jet is similar to that conceived by Shibata & Uchida (1986). There are some important differences between these early suggestions and our current work, however. First, our simulations produce both the quasi-steady tapered outflow and the subsequent impulsive jet in the absence of any flux

emergence whatsoever. This suggests that these features of mini-filament jets, at least, may be universal and occur irrespective of whether flux is emerging within the jet source region. Second, there is positive feedback between the expansion of the filament channel field below the BCS and

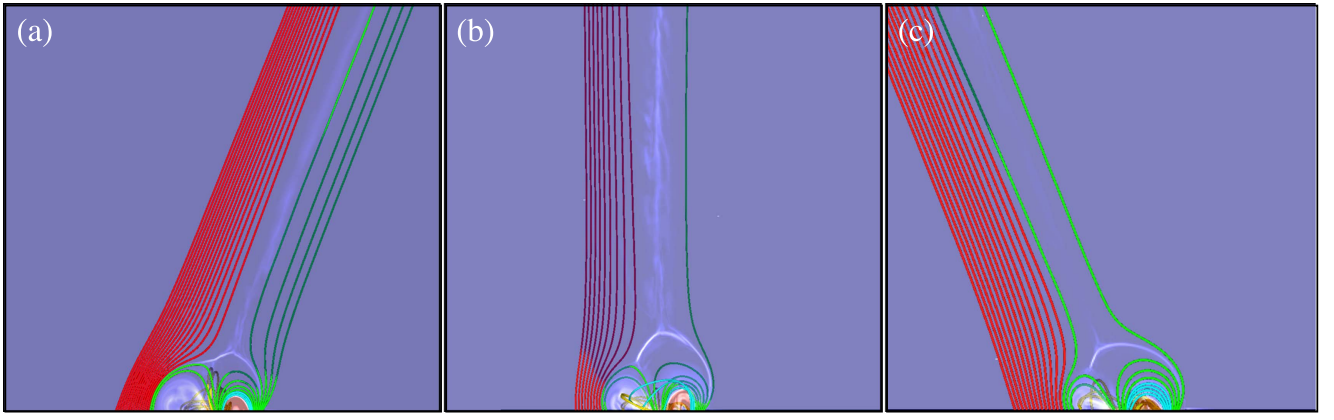


Figure 13. Post-jet magnetic field. (a) $\theta = +22^\circ$, $t = 49$ minutes 20 s; (b) $\theta = 0^\circ$, $t = 66$ minutes 40 s; (c) $\theta = -22^\circ$, $t = 54$ minutes. Shading shows the nondimensional electric current density $|J|$ ($\times 1.5 \times 10^{-3} \text{ A m}^{-2}$ with coronal scalings).

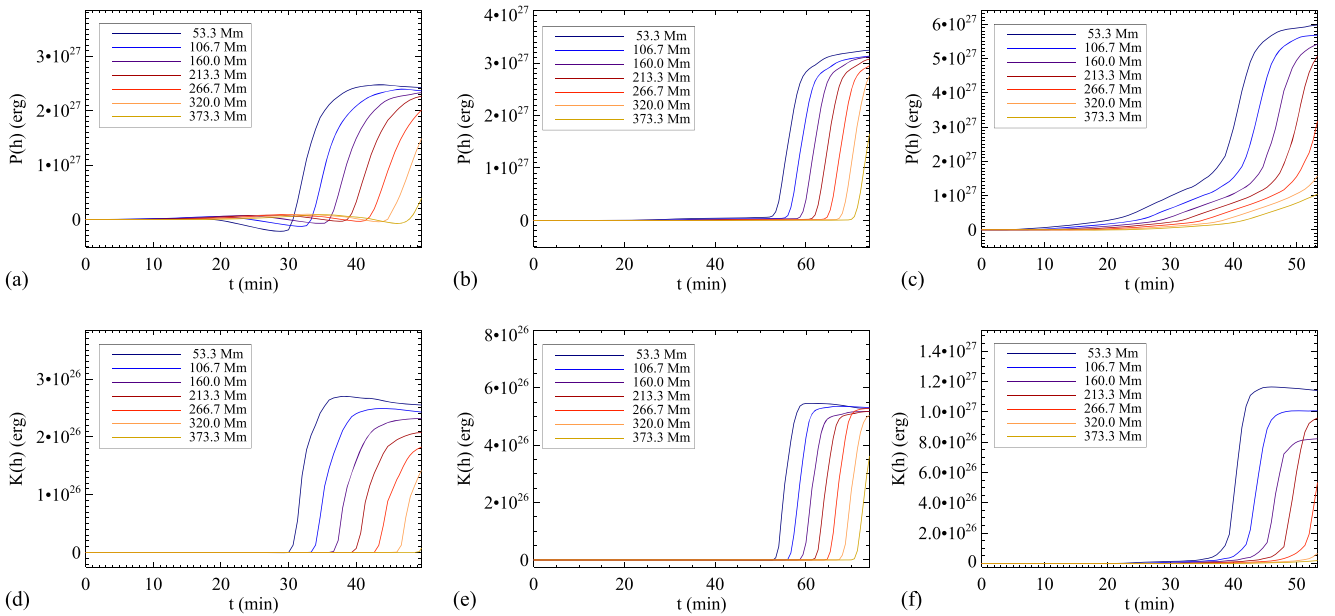


Figure 14. Top: cumulative Poynting flux $P(h)$ across surfaces at selected heights h above the photosphere. Bottom: cumulative kinetic-energy flux $K(h)$ across the same surfaces. (a) and (d): $\theta = +22^\circ$; (b) and (e): $\theta = 0^\circ$; (c) and (f): $\theta = -22^\circ$. Note the different vertical and horizontal scales used in each graph.

the interchange reconnection of the strapping field across it. This is a key feature of the magnetic-breakout mechanism (Antiochos et al. 1999) and provides the energy release needed to accelerate the explosive breakout reconnection process. Third, we find that the site of interchange (open/closed) reconnection moves from the BCS above the mini-filament flux rope to the initially slowly reconnecting current sheet below it, leading to the onset of explosive flare reconnection during the jet. This transition simultaneously launches the multithermal Alfvénic jet and produces the hot flare loops corresponding to the jet bright point.

The early Shibata models envisioned only a single current sheet, formed at the interface between the emerging (closed) and ambient (open) magnetic flux systems, so that the jet and the flare always would be in very close proximity to one another. In our model, the free magnetic energy is introduced by shearing the field along the PIL of the embedded bipolar region. The strong shear at the center of the bipole induces reconnection near the photosphere that creates a flux rope in two of the configurations prior to the onset of the breakout

phase. However, this weak tether-cutting reconnection (Moore & Roumeliotis 1992; Moore et al. 2001) neither significantly releases any of the stored energy nor initiates the eruption. More rapid tether-cutting reconnection occurred once the breakout phase began and the flux rope began to rise as the strapping field was removed from above, as is expected in both the tether-cutting and breakout pictures. Thus, although tether cutting is certainly involved, and in fact is crucial for converting the shear in the filament channel field to twist within the flux rope, it is not the driver of our jets.

This internal reconnection seems to play an important role in suppressing the global kinking of the closed field, which occurs in the kink-initiated jet models of Pariat and coworkers (e.g., Pariat et al. 2009). We estimated the number of turns that could theoretically be achieved in our simulations by tracing field lines from the photosphere at a time prior to the onset of internal reconnection, assessing the highest number of turns at this point, and extrapolating it to the full duration of the footpoint driving. The number of turns was $N \approx 1.2, 0.9$, and 0.7 for $\theta = -22^\circ, 0^\circ$, and $+22^\circ$, respectively, within the range

of $N = 0.8$ – 1.4 found by Parlat et al. (2010) to set off a kink. Nevertheless, we observed no global kinking. Nor was any obvious writhe or rotation of the flux rope observed, as is thought to trigger some large-scale filament eruptions (Török & Kliem 2005).

The ideal torus instability (Kliem & Török 2006) is frequently cited as explaining the eruption of flux ropes in bipolar magnetic fields. The instability assumes a preexisting flux rope and occurs in bipolar fields where the strapping field strength drops off faster than a critical threshold. In the magnetic configuration for our simulations, the background-field strength is uniform, negating this instability well away from our closed-field region. Within the closed-field region, the field strength does drop off toward the null but then increases again beyond it. It is not clear whether the torus instability could operate in this configuration; an ideal treatment of the evolution would be necessary to be definitive. In any case, it is certain that the dynamics in our simulations are dominated by the nonideal evolution of the breakout and flare current sheets, and these dynamics are at the heart of the eruptive-jet generation.

Finally, we note that some flux emergence experiments (e.g., Archontis & Hood 2013) have exhibited an evolution in the untwisting jets they produce similar to those from our model. Our breakout process relies rather generically on the storage of free energy within the magnetic topology of a null point above a strong bipolar field. In the observations and in our model, the null point and bipole are preexisting. However, the same topology can be created dynamically by flux emergence, as occurs in the Archontis & Hood numerical experiments. Indeed, even large-scale breakout CMEs can be realized in flux emergence experiments when the overlying field is correctly aligned (e.g., Archontis & Török 2008; Hood et al. 2012; Leake et al. 2014). Thus, our model provides a rather general framework for interpreting events where free energy is stored along the PIL of a bipole in a null point topology. In principle, this storage could occur as a result of flux emergence, surface motions, or even flux cancellation. Once the free energy is stored there, the subsequent breakout behavior is expected to be more or less the same.

7.3. Summary

In this work we have described in detail a new model for coronal jets involving mini-filament eruptions. Our model extends the well-known breakout model for large-scale CMEs (Antiochos 1998; Antiochos et al. 1999) to these much smaller events (Wyper et al. 2017) and explains a number of their observed features.


In our model, free energy is stored in a filament channel along the PIL of a preexisting bipole. The sheared filament channel erupts as the jet is launched via the breakout process. Following on from the initial study of Wyper et al. (2017), we studied three realizations of the model with varying background-field inclinations and found the breakout mechanism to work robustly in each case. In configurations where the field is highly inclined to the vertical, the breakout reconnection produces an inverted-Y-type reconnection outflow, similar in nature to outflows observed prior to mini-filament jets in similar configurations. This outflow was much weaker when the field is vertical. In all configurations, a broad untwisting jet is realized when the flux rope formed during the breakout phase reaches the BCS. Our jet is a combination of an untwisting flux

rope and impulsive interchange reconnection in the flare current sheet formed below the flux rope. Flare loops created by the low-lying reconnection in our model correspond to the jet bright point. The majority of the energy transmitted to the open field of the corona is in the form of a Poynting flux associated with a nonlinear torsional Alfvén wave, which is launched by reconnection between the twisted internal flux rope and the untwisted external field. Our findings highlight the similarities between eruptive events across different scales in the solar atmosphere and demonstrate the universality of the breakout mechanism for explaining them (Wyper et al. 2017).

In future work, we aim to assess how our model performs when effects such as gravitational stratification and heating terms are included. Further understanding of the magnetic topology and its relation to flare brightening and high-energy particles is also expected to give valuable insight into these events.

This work was supported through P.F.W.’s award of a Royal Astronomical Society Fellowship and also through C.R.D.’s and S.K.A.’s participation in NASA’s Living With a Star and Heliophysics Supporting Research programs. Computer resources for the numerical simulations were provided to C.R.D. by NASA’s High-End Computing program at the NASA Center for Climate Simulation. We are grateful to J. T. Karpen, P. Kumar, C. E. DeForest, N. E. Raouafi, V. M. Uritsky, and M. A. Roberts for numerous helpful discussions of jets and their observations.

ORCID iDs

P. F. Wyper  <https://orcid.org/0000-0002-6442-7818>
C. R. DeVore  <https://orcid.org/0000-0002-4668-591X>
S. K. Antiochos  <https://orcid.org/0000-0003-0176-4312>

References

- Adams, M., Sterling, A. C., Moore, R. L., & Gary, G. A. 2014, *ApJ*, **783**, 11
- Antiochos, S. K. 1998, *ApJL*, **502**, L181
- Antiochos, S. K., Dahlburg, R. B., & Klimchuk, J. A. 1994, *ApJL*, **420**, L41
- Antiochos, S. K., DeVore, C. R., & Klimchuk, J. A. 1999, *ApJ*, **510**, 485
- Archontis, V., & Hood, A. W. 2013, *ApJL*, **769**, L21
- Archontis, V., Moreno-Insertis, F., Galsgaard, K., & Hood, A. W. 2005, *ApJ*, **635**, 1299
- Archontis, V., & Török, T. 2008, *A&A*, **492**, L35
- Archontis, V., Tsinganos, K., & Gontikakis, C. 2010, *A&A*, **512**, L2
- Aulanier, G., DeVore, C. R., & Antiochos, S. K. 2002, *ApJL*, **567**, L97
- Canfield, R. C., Reardon, K. P., Leka, K. D., et al. 1996, *ApJ*, **464**, 1016
- Chae, J., Qiu, J., Wang, H., & Goode, P. R. 1999, *ApJL*, **513**, L75
- Chandrasekhar, K., Morton, R. J., Banerjee, D., & Gupta, G. R. 2014, *A&A*, **562**, A98
- Cirtain, J. W., Golub, L., Lundquist, L., et al. 2007, *Sci.*, **318**, 1580
- Dalmasse, K., Parlat, E., Antiochos, S. K., & DeVore, C. R. 2012, in *EAS Publications Ser. 55, Understanding Solar Activity: Advances and Challenges*, ed. M. Faurobert, C. Fang, & T. Corbard (Paris: EDP), 201
- DeVore, C. R., & Antiochos, S. K. 2000, *ApJ*, **539**, 954
- DeVore, C. R., & Antiochos, S. K. 2008, *ApJ*, **680**, 740
- Fang, F., Fan, Y., & McIntosh, S. W. 2014, *ApJL*, **789**, L19
- Galsgaard, K., Moreno-Insertis, F., Archontis, V., & Hood, A. 2005, *ApJL*, **618**, L153
- Gontikakis, C., Archontis, V., & Tsinganos, K. 2009, *A&A*, **506**, L45
- Hong, J., Jiang, Y., Yang, J., et al. 2014, *ApJ*, **796**, 73
- Hong, J., Jiang, Y., Yang, J., et al. 2016, *ApJ*, **830**, 60
- Hong, J., Jiang, Y., Zheng, R., et al. 2011, *ApJL*, **738**, L20
- Hong, J.-C., Jiang, Y.-C., Yang, J.-Y., et al. 2013, *RAA*, **13**, 253
- Hood, A. W., Archontis, V., & MacTaggart, D. 2012, *SoPh*, **278**, 3
- Innes, D. E., Genetelli, A., Attie, R., & Potts, H. E. 2009, *A&A*, **495**, 319
- Innes, D. E., McIntosh, S. W., & Pietarila, A. 2010, *A&A*, **517**, L7
- Karpen, J. T., Antiochos, S. K., & DeVore, C. R. 2012, *ApJ*, **760**, 81

- Karpen, J. T., Antiochos, S. K., Hohensee, M., Klimchuk, J. A., & MacNeice, P. J. 2001, [ApJL](#), **553**, L85
- Karpen, J. T., DeVore, C. R., Antiochos, S. K., & Pariat, E. 2017, [ApJ](#), **834**, 62
- Karpen, J. T., Tanner, S. E. M., Antiochos, S. K., & DeVore, C. R. 2005, [ApJ](#), **635**, 1319
- Kliem, B., & Török, T. 2006, [PhRvL](#), **96**, 255002
- Leake, J. E., Linton, M. G., & Antiochos, S. K. 2014, [ApJ](#), **787**, 46
- Liu, W., Berger, T. E., Title, A. M., Tarbell, T. D., & Low, B. C. 2011, [ApJ](#), **728**, 103
- Luna, M., Karpen, J. T., & DeVore, C. R. 2012, [ApJ](#), **746**, 30
- Lynch, B. J., Antiochos, S. K., DeVore, C. R., Luhmann, J. G., & Zurbuchen, T. H. 2008, [ApJ](#), **683**, 1192
- Lynch, B. J., Antiochos, S. K., Li, Y., Luhmann, J. G., & DeVore, C. R. 2009, [ApJ](#), **697**, 1918
- MacNeice, P., Antiochos, S. K., Phillips, A., et al. 2004, [ApJ](#), **614**, 1028
- MacNeice, P., Olson, K. M., Mobarry, C., de Fainchtein, R., & Packer, C. 2000, [CoPhC](#), **126**, 330
- Masson, S., Antiochos, S. K., & DeVore, C. R. 2013, [ApJ](#), **771**, 82
- Masson, S., Aulanier, G., Pariat, E., & Klein, K.-L. 2012, [SoPh](#), **276**, 199
- Miyagoshi, T., & Yokoyama, T. 2003, [ApJL](#), **593**, L133
- Miyagoshi, T., & Yokoyama, T. 2004, [ApJ](#), **614**, 1042
- Moore, R. L., Cirtain, J. W., Sterling, A. C., & Falconer, D. A. 2010, [ApJ](#), **720**, 757
- Moore, R. L., & Roumeliotis, G. 1992, in IAU Coll. 133: Eruptive Solar Flares, ed. Z. Svestka, B. V. Jackson, & M. E. Machado (Berlin: Springer), 69
- Moore, R. L., Sterling, A. C., & Falconer, D. A. 2015, [ApJ](#), **806**, 11
- Moore, R. L., Sterling, A. C., Hudson, H. S., & Lemen, J. R. 2001, [ApJ](#), **552**, 833
- Moreno-Insertis, F., & Galsgaard, K. 2013, [ApJ](#), **771**, 20
- Moreno-Insertis, F., Galsgaard, K., & Ugarte-Urra, I. 2008, [ApJL](#), **673**, L211
- Nisticò, G., Bothmer, V., Patsourakos, S., & Zimbardo, G. 2009, [SoPh](#), **259**, 87
- Panesar, N. K., Sterling, A. C., Moore, R. L., & Chakrapani, P. 2016, [ApJL](#), **832**, L7
- Pariat, E., Antiochos, S. K., & DeVore, C. R. 2009, [ApJ](#), **691**, 61
- Pariat, E., Antiochos, S. K., & DeVore, C. R. 2010, [ApJ](#), **714**, 1762
- Pariat, E., Dalmasse, K., DeVore, C. R., Antiochos, S. K., & Karpen, J. T. 2015, [A&A](#), **573**, A130
- Pariat, E., Dalmasse, K., DeVore, C. R., Antiochos, S. K., & Karpen, J. T. 2016, [A&A](#), **596**, A36
- Patsourakos, S., Pariat, E., Vourlidas, A., Antiochos, S. K., & Wuelser, J. P. 2008, [ApJL](#), **680**, L73
- Phillips, A. D., MacNeice, P. J., & Antiochos, S. K. 2005, [ApJL](#), **624**, L129
- Pontin, D. I., Bhattacharjee, A., & Galsgaard, K. 2007, [PhPl](#), **14**, 052106
- Raouafi, N.-E., Georgoulis, M. K., Rust, D. M., & Bernasconi, P. N. 2010, [ApJ](#), **718**, 981
- Raouafi, N. E., Patsourakos, S., Pariat, E., et al. 2016, [SSRv](#), **201**, 1
- Savcheva, A., Cirtain, J., Deluca, E. E., et al. 2007, [PASJ](#), **59**, 771
- Shen, Y., Liu, Y., Su, J., & Ibrahim, A. 2011, [ApJL](#), **735**, L43
- Shibata, K., Ishido, Y., Acton, L. W., et al. 1992, [PASJ](#), **44**, L173
- Shibata, K., & Uchida, Y. 1986, [SoPh](#), **103**, 299
- Shimojo, M., Hashimoto, S., Shibata, K., et al. 1996, [PASJ](#), **48**, 123
- Sterling, A. C., Moore, R. L., Falconer, D. A., & Adams, M. 2015, [Natur](#), **523**, 437
- Titov, V. S. 2007, [ApJ](#), **660**, 863
- Titov, V. S., Hornig, G., & Démoulin, P. 2002, [JGRA](#), **107**, 1164
- Török, T., & Kliem, B. 2005, [ApJL](#), **630**, L97
- van Ballegooijen, A. A., & Martens, P. C. H. 1989, [ApJ](#), **343**, 971
- Wang, Y.-M., Sheeley, N. R., Jr., Socker, D. G., et al. 1998, [ApJ](#), **508**, 899
- Wyper, P. F., Antiochos, S. K., & DeVore, C. R. 2017, [Natur](#), **544**, 452
- Wyper, P. F., & DeVore, C. R. 2016, [ApJ](#), **820**, 77
- Wyper, P. F., DeVore, C. R., Karpen, J. T., & Lynch, B. J. 2016, [ApJ](#), **827**, 4
- Wyper, P. F., & Pontin, D. I. 2014a, [PhPl](#), **21**, 082114
- Wyper, P. F., & Pontin, D. I. 2014b, [PhPl](#), **21**, 102102
- Yokoyama, T., & Shibata, K. 1995, [Natur](#), **375**, 42
- Yokoyama, T., & Shibata, K. 1996, [PASJ](#), **48**, 353
- Young, P. R., & Muglach, K. 2014a, [PASJ](#), **66**, S12
- Young, P. R., & Muglach, K. 2014b, [SoPh](#), **289**, 3313
- Zhang, Q. M., Li, D., Ning, Z. J., et al. 2016, [ApJ](#), **827**, 27
- Zheng, R., Jiang, Y., Yang, J., et al. 2012, [ApJ](#), **753**, 112